Pure shear deformation of square objects, and applications to geological strain analysis

Susan H. Treagus[a],*, Labao Lan[b, 1]

[a]*Department of Earth Sciences, University of Manchester, Manchester M13 9PL, UK*
[b]*Department of Geology and Geophysics, University of Minnesota, Minneapolis, MN 55455, USA*

Abstract

Geological objects that deform differently from the rock matrix, such as pebbles or other clasts, are unlikely to have been originally circular or elliptical in section, and must therefore be expected to deform heterogeneously and change shape irregularly. We investigate this process with finite element models of pure shear deformation of square objects in three orientations, square, skew and diagonal, in a matrix with different viscosity. Modelling shows that 'squares' deform irregularly, with competent objects becoming barrel shaped and 'fish mouthed' (cf. boudins), whereas incompetent objects become bone shaped or elongate lobes. The object aspect ratios (R_O) are less different from the bulk strain ratio (R_S) than for equivalent circular objects. In contrast, diagonal squares deform almost homogeneously into 'rhombs', with aspect ratios closer to those for circles. Asymmetrically oriented 'skew squares' behave intermediately, developing skew flag and hooked shapes according to competence contrasts, that might be misdiagnosed as shear criteria.

All these square objects (and circles in theory), show almost linear strain paths of object versus bulk $(R-1)$, with slope related to viscosity ratio, object shape and orientation. Linear relationships are also found for concavity/convexity shape factors for 'squares'. The results have implications for strain analysis and competence contrasts in rocks. © 1999 Elsevier Science Ltd. All rights reserved.

1. Introduction

To quantify the deformation in rocks, structural geologists need geological markers on which to perform strain analysis (Ramsay and Huber, 1983). Ideal *strain markers* might be those that represent the total strain of the rock on a certain scale, and which can also provide a direct strain measurement. 'Reduction' spots, ooliths and volcanic lapilli might all be considered to be in this category: objects of supposedly initial spherical shape that deform to ellipsoids presumed to be representative of the strain ellipsoid for the rock. Such strain markers, however, are relatively rare; they do not conveniently occur all throughout the geological succession, or over a map area. So, in practice, geo-

logical strain analysis is likely to be based on less perfect strain markers, such as deformed pebbles or other kinds of clast. Because of their relatively common occurrence in the stratigraphic succession, deformed conglomerates have historically provided one of the most important databases for strain analysis (Flinn, 1956; Hossack, 1968; see Ramsay and Huber, 1983, pp. 297–300 for source literature).

There are two broad approaches to strain studies of deformed conglomerates and similar clast–matrix systems. Both, however, make the assumption that the pebbles or clasts can be considered initially to have been spherical or ellipsoidal (thus, in two-dimensional studies, circular or elliptical). The first and most common approach is to assume a *homogeneous deformation* of the pebbles and matrix, so that the statistical information on pebble axial ratios and orientations can yield a measurement of strain, an example being $R_f–\phi$ analyses of conglomerates (see Lisle, 1985; and refer-

* Corresponding author.

[1] IRI/Lamont-Doherty Earth Observatory, Columbia University, Palisades, NY 10964-8000, USA.

ences therein). The second approach is to utilise the *competence contrasts* between pebbles and their surrounding matrix, and consider these rocks as object–matrix systems: the concern of this paper.

1.1. Object–matrix systems

It has been shown from two-dimensional theory (Eshelby, 1957; Gay, 1968a; Bilby et al., 1975), that isolated elliptical markers in a matrix of different viscosity will deform homogeneously into ellipses, but with strain ratios different from the bulk strain ratio, according to the viscosity contrast. For initially *circular* objects in pure shear, the theoretical results in Bilby et al. (1975) can be given explicitly, as

$$\ln R_S = \ln R_O + \{(m-1)(R_O-1)/(R_O+1)\}, \qquad (1)$$

where R_S is the bulk strain axial ratio, R_O is the inclusion or object strain ratio, and m is the viscosity ratio of object to matrix.

The strain relationship given in Eq. (1), can be illustrated graphically as a set of curves of R_O versus R_S, for different m values, usually on a log–log scale (e.g. Bilby et al., 1975; also Gay, 1976; Treagus et al., 1996) (see later Fig. 11d). While the theoretical approaches of Gay (1968a) and Bilby et al. (1975) are subtly different, the results for geologically reasonable values of bulk strain can be shown to be virtually the same (Gay, 1976). The m-curves drawn from Eq. (1) for circular objects are slightly non-linear for bulk strain ratios up to 10 or 20 (linearity would imply a steady incremental change). Competent objects ($m > 1$) have very slightly increasing $\ln R_O/\ln R_S$; incompetent objects ($m < 1$) more measurably show a decreasing $\ln R_O/\ln R_S$ with increasing R_S. These trends are more clearly seen in Bilby et al. (1975, fig. 2) as curves that become subparallel at high bulk strain, which mean that with increasing bulk and object strain, elliptical objects deform by increments that increasingly approach the bulk strain increments. These results will be returned to, later in the paper.

The theoretical analyses of Eshelby (1957) and Bilby et al. (1975) treated object–matrix systems as two-dimensional, by considering the objects as circular or elliptical cylinders in three dimensions; but the latter paper also considered deformation of prolate and oblate spheroids. Freeman (1987) developed the theory to consider the effects of triaxial strain on spherical and ellipsoidal objects, and their implications for geological strain analysis. Importantly, he demonstrated that competent spherical objects would deform to more prolate shapes than the bulk strain ellipsoid, more so at higher m. Incompetent objects were not considered, but it might be reasonable to suppose these showed reciprocal effects of more oblate strain.

Gay (1968a) and Bilby and Kolbuszewski (1977) considered the effects of both pure and simple shear flows, and the latter leads into modelling of oscillatory flow, a subject that will not be reviewed further here. The present paper will investigate two dimensions, only, and will be concerned with pure shear (plane strain).

Finite element modelling of the deformation of circular objects in a contrasting matrix, by Shimamoto (1975), confirmed the theory. Although presented as confirmation of Gay's (1968a) equation, Shimamoto's results confirm just as well the contemporaneous results of Bilby et al. (1975) (Eq. 1), since these are virtually the same until excessively high strain. These numerical models also demonstrate strain trajectory patterns that arise in the matrix surrounding more competent and less competent objects. The bowing of extensional trajectories around stiffer objects is analogous to patterns of cleavage wrapping round supposedly more competent geological objects (e.g. clasts), commonly used by field geologists to indicate competence contrasts (see, for example, Lisle, 1985, fig. 5.1).

The theory reviewed above has been applied to deformed conglomerates by Gay (1968b), Gay and Fripp (1976), and Lisle et al. (1983). By comparing strain measurements from single pebbles or statistically for groups of like lithology, these analyses are able to deduce viscosity contrasts among rock-types, which turn out to be quite small numerical values (e.g. 2, and 9 at maximum). These applications are all based on modelling pebbles as initially circular or elliptical in shape. In Treagus et al. (1996), we questioned whether this should be *generally* assumed for clast shapes. If geological clasts such as pebbles in conglomerate are not approximately ellipsoidal, how would their real shape affect their deformation, and how might this be modelled?

1.2. Non-circular and non-elliptical objects in a matrix

In Treagus et al. (1996), we introduced this topic by reviewing whether most grains, pebbles and other clasts in rocks are sufficiently 'round' to be viably modelled as circular (or elliptical) in section. Evidence suggests that even pebbles described as 'round', might be better approximated as super-ellipsoids with axial symmetry (Lisle, 1988), and many types of geological clasts are much more angular. The theory reviewed above states that circular objects in a contrasting matrix deform homogeneously into variably elongate ellipses, according to the bulk strain and viscosity ratio (Eq. 1). The converse, implicit in Eshelby (1957) and Bilby et al. (1975), is that non-elliptical objects with viscosity contrast will *not* deform homogeneously, and therefore will *not* maintain a regular shape. We demonstrated this in Treagus et al. (1996, fig. 3), by presenting finite-element models of square objects in a matrix, in pure shear (50% shortening) oriented paral-
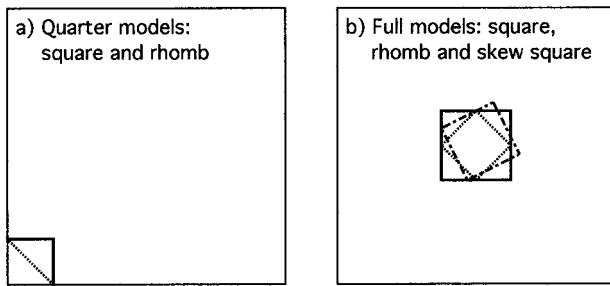
Fig. 1. Previous and new designs of object–matrix finite element models, scaled to match. (a) Quarter models, as used in Treagus et al. (1996). (b) Full models used for this paper. 'Square' is shown with solid lines, 'rhomb' with dotted lines, and 'skew square' in dot–dash lines. The outer square marks the whole model.

lel or diagonal to the square. The models differed from Selkman's (1983), who concentrated on deformation and stress variations within and around stiff square objects shortened only up to 8.33%. Our models had a wide range of viscosity ratios, including incompetent objects ($m < 1$).

The square competent objects ($1 < m < 10$) became barrel-shaped (Treagus et al., 1996, fig. 3a), and may be likened to geological boudins (Ramberg, 1955; Ghosh and Ramberg, 1976). These shapes were similar to, but less extreme than, those produced in elastic–plastic finite element models of boudinage by Lloyd and Ferguson (1981). Our square incompetent objects ($m < 1$) became bone shaped to smoothly elongate lobes that virtually eradicated the initial shape. In contrast, our second set of models with diagonal square objects (Treagus et al., 1996, fig. 3b), produced much less shape irregularity (even less than these drawings suggested), and were all approximately rhombic. From this preliminary modelling, we also speculated about the deformation of square objects in other orientations, other deformation histories, and shapes between square and circular. This has developed into a wider-reaching research project on numerical modelling of deformation of non-ellipsoidal objects with competence contrast, and their geological significance, especially to the deformation of fragmental rocks. This paper reports some of the new model results.

2. Finite element modelling

We use a two-dimensional finite element program for slow (quasi-static) flow of an incompressible fluid. The finite element code was developed (Hanson, 1990) to model ice sheet deformation as an incompressible power-law fluid. The code has been modified and applied to structural analysis of folding and thrusting deformation in Newtonian and power-law systems by Lan and Hudleston (1991, 1996, 1997; Hudleston and

Lan, 1994). It was used to model deformation of isolated objects in a contrasting matrix by Treagus et al. (1996) and in this paper, where both object and matrix are assumed to be Newtonian fluids with constant viscosity ratio.

These first results (Treagus et al., 1996) came from *quarter models* due to symmetry, but are only suitable for modelling two orientations (square and diagonal-square) (Fig. 1a). The new models presented here are *full models*, suitable for objects with symmetry or asymmetry in orientation and shape (Fig. 1b). The object is constructed in the centre, and a variety of shapes and orientations, square and rectangular, can be created within the basic grid. This paper concentrates on squares, in three orientations (Fig. 1b).

The *full square model* has the square object aligned with pure shear axes. It comprises 409 nodes and 416 elements, of which 236 are linear convex quadrilaterals, and 80 are transitional triangles (Fig. 2a). To produce more accurate strain simulations, the object is dissected into smaller quadrilateral elements, which are defined to have a viscosity of type 2, compared to the rest of the model that is type 1 (see dashed boundaries, Fig. 2). This model has a linear object/matrix ratio of 1/4, and area ratio of 1/16, making it somewhat further from the 'theoretical object in a semi-infinite matrix', than the quarter model. Its design, however, is considered to optimise two variables: (1) the need for sufficient matrix to surround the object and accommodate the heterogeneous matrix strain; (2) the need to make an object with sufficient nodes and elements to model irregular shape development accurately. These two factors are to some extent conflicting, especially if there are other practical considerations, such as overall model size and the resulting running times. The finite element grid is shown in Fig. 2, together with results for viscosity ratios of 5 and 0.2 at 50% shortening.

A *diagonal square* full model was also created (Fig. 1b), called *rhomb* (comparable to the quarter rhomb). However, the main purpose of the new design was to deform objects that are oblique and asymmetric in pure shear. The *skew square model* (Fig. 1b) is thus constructed, drawn within the central area across 2:1 triangles, such that the sides are inclined at $\tan^{-1} = 2$ and 0.5 ($26.6°$ and $63.4°$) to the bulk pure shear. This skew square model comprises 409 nodes and 440 elements.

The boundary conditions for pure shear are a 'horizontal' velocity component for the nodes along the right vertical edge of the grid, and zero horizontal velocity for the nodes along the left vertical edge. Vertical velocities at these nodes were free. The vertical and horizontal velocities at the nodes along the bottom of the model were set to zero and free, respectively. No constraints were placed on the top boundary of the models, and there are accordingly some deflections of this boundary, apparent in Fig. 2. These are not found

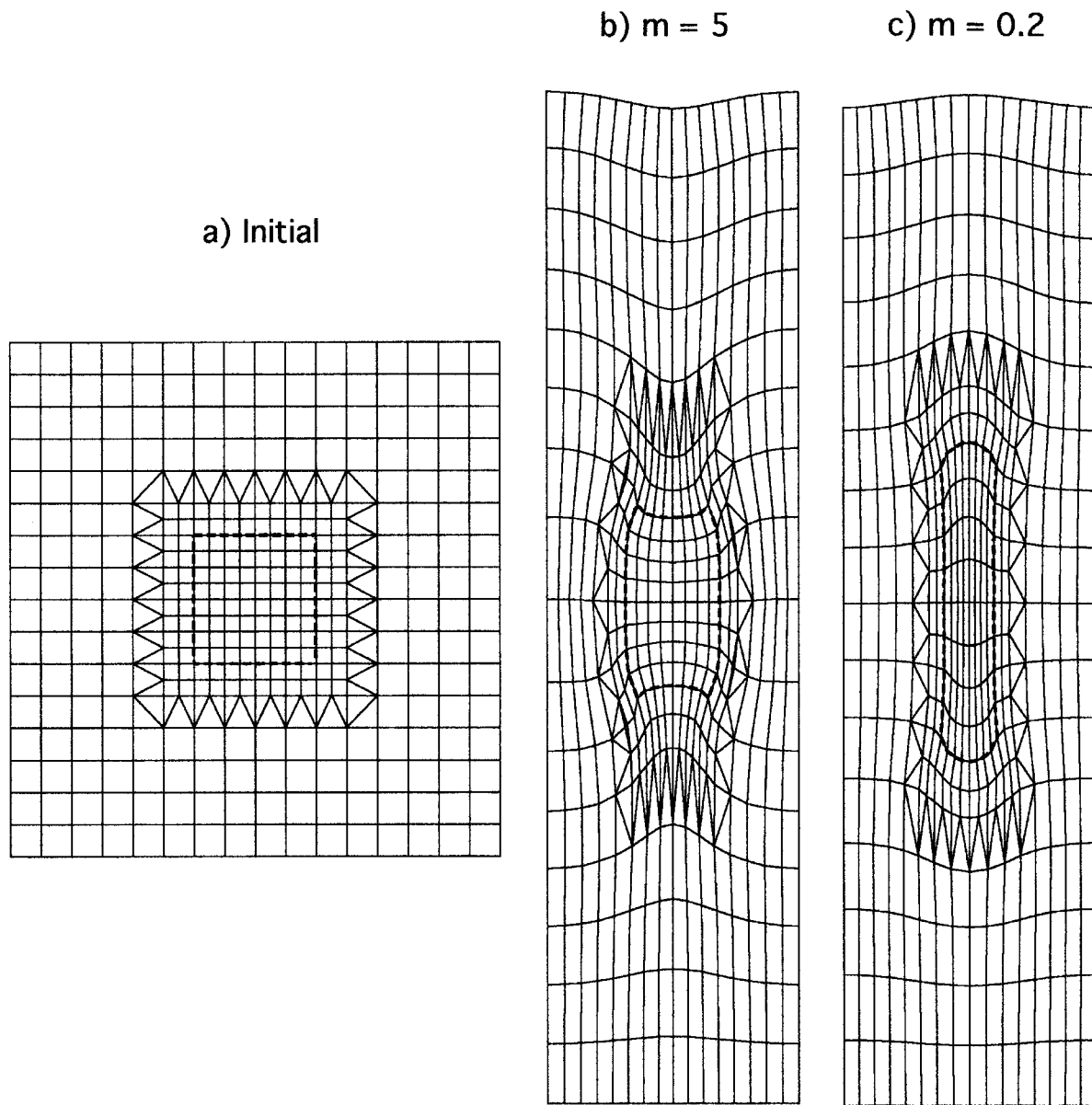## b) m = 5   c) m = 0.2

a) Initial

Fig. 2. The new full model showing the finite element grid. (a) Initial configuration, with dashed boundary showing the change from material type 1 (matrix) to type 2 (object) for the 'squares' series. (b) and (c) Models deformed by $R = 4$ (50% shortening), with viscosity ratio m (type2: type1) = 5 and 0.2.

to impose any significant effect in the central regions, sufficient to result in differences between upper and lower object edge shapes. The velocities at all nodes are calculated for the initial mesh and boundary conditions. The time increment was used to update nodal co-ordinates during pure shear deformation. Each time increment is 0.025 units, with units of length and time non-dimensionalised. The whole model in our study is initially 3.2 units square, and so a 50% shortening (bulk strain axial ratio, $R = 4$) is achieved in 64 time increments (t). The results for these three types of full models are presented for four deformation stages: 25%

shortening ($R = 1.78$; $t = 32$), 50% ($R = 4$; $t = 64$), 67% ($R = 9.2$; $t = 86$) and 75% ($R = 16$; $t = 96$).

3. Model results

Finite element results are presented in Figs. 3–7, for the three designs of full models of square objects in a matrix, for selected viscosity ratios. In this paper, we will concentrate on the *shapes* of the deformed objects, and ways of quantifying their *average strain*. Each figure compares full square, skew square and rhomb models, progressing upwards from the initial square through the
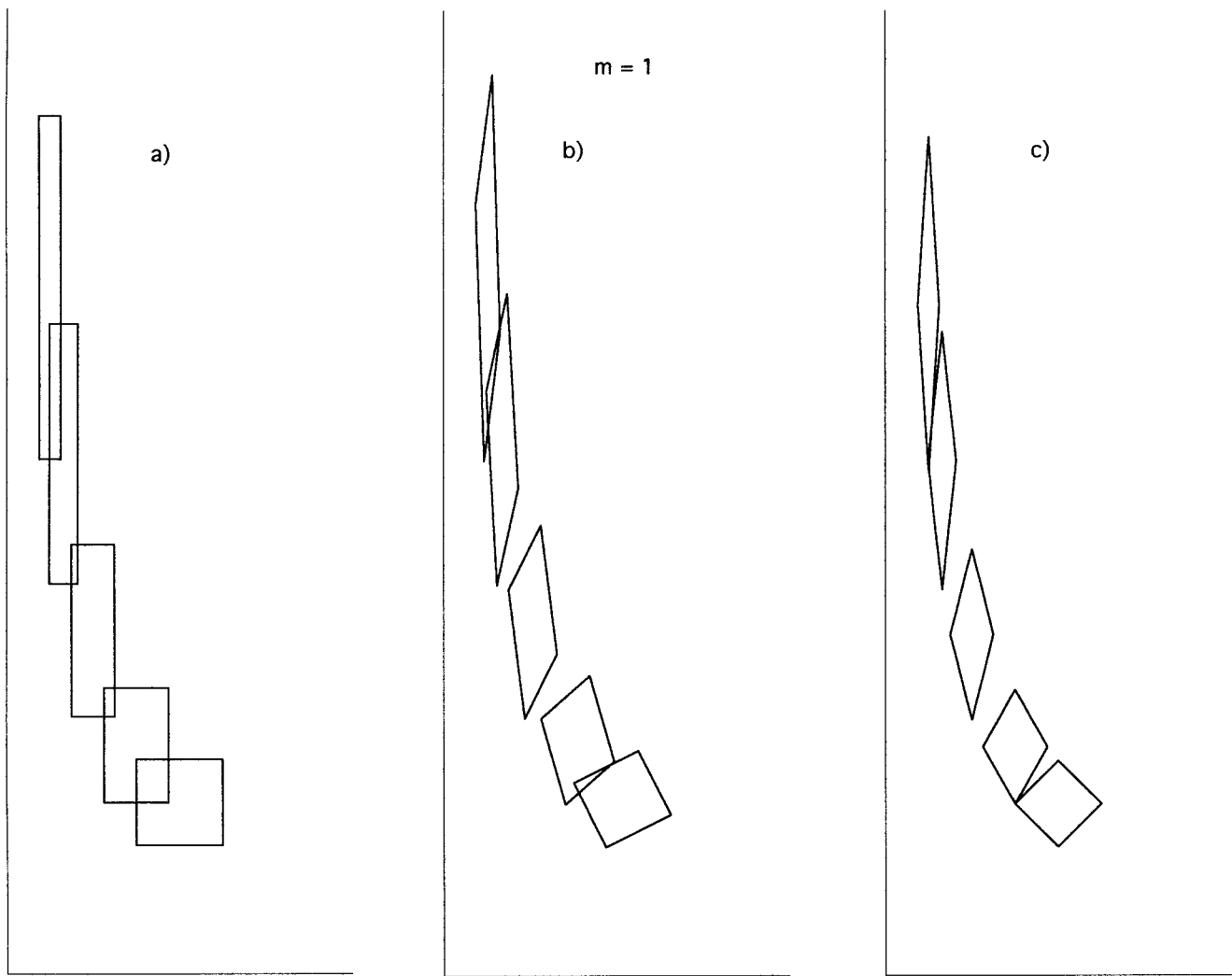
Fig. 3. Shapes of deformed square objects in a matrix, oriented as (a) 'square', (b) 'skew square' and (c) 'rhomb'. Bottom rows show initial shapes; successive rows upwards are the four model deformation stages, $R = 1.78$, 4, 9.18 and 16. $m = 1$, which is passive behaviour.

four stages of deformation. The object co-ordinate positions are given with respect to the bottom and left model edges (see also Figs. 1b and 2). Fig. 3 presents models with no viscosity contrast ($m = 1$), equivalent to homogeneous strain of passive square markers in three orientations. Note that the decreases in linear dimensions of object and matrix, in the shortening direction, are in step; thus, the linear object/matrix ratio of 1/4 is unchanged and non-directional throughout deformation. This is not the case, where $m \neq 1$.

Figs. 4–7 demonstrate the differences in object strain and orientation with viscosity ratio, m, for comparison with Fig. 3. The characteristic features for competent and incompetent objects will be discussed separately, below. However, reasons for showing three models of competent objects, but only one of incompetent, should first be explained. Many more models (not shown), and their measurements (shown in later figures), demon-

strate surprisingly small differences in results for $m < 1$, over several orders of m-magnitude. In contrast, the differences for competent objects are more distinctive and significant, and we argue later that these may have geological applications. The following descriptions concern qualitative features, and these will be addressed quantitatively in subsequent sections.

3.1. Competent objects

Figs. 4–6 provide model results for $m = 100$, 10 and 5, for mutual comparison. For $m = 100$ (Fig. 4), up to 50% model shortening (middle row) the objects all show very little deformation, behaving almost rigidly. The skew squares show no rotation, confirming what would be expected for rigid equant objects in a deformation with zero vorticity (Ghosh and Ramberg, 1976). However, during the last two stages of defor-
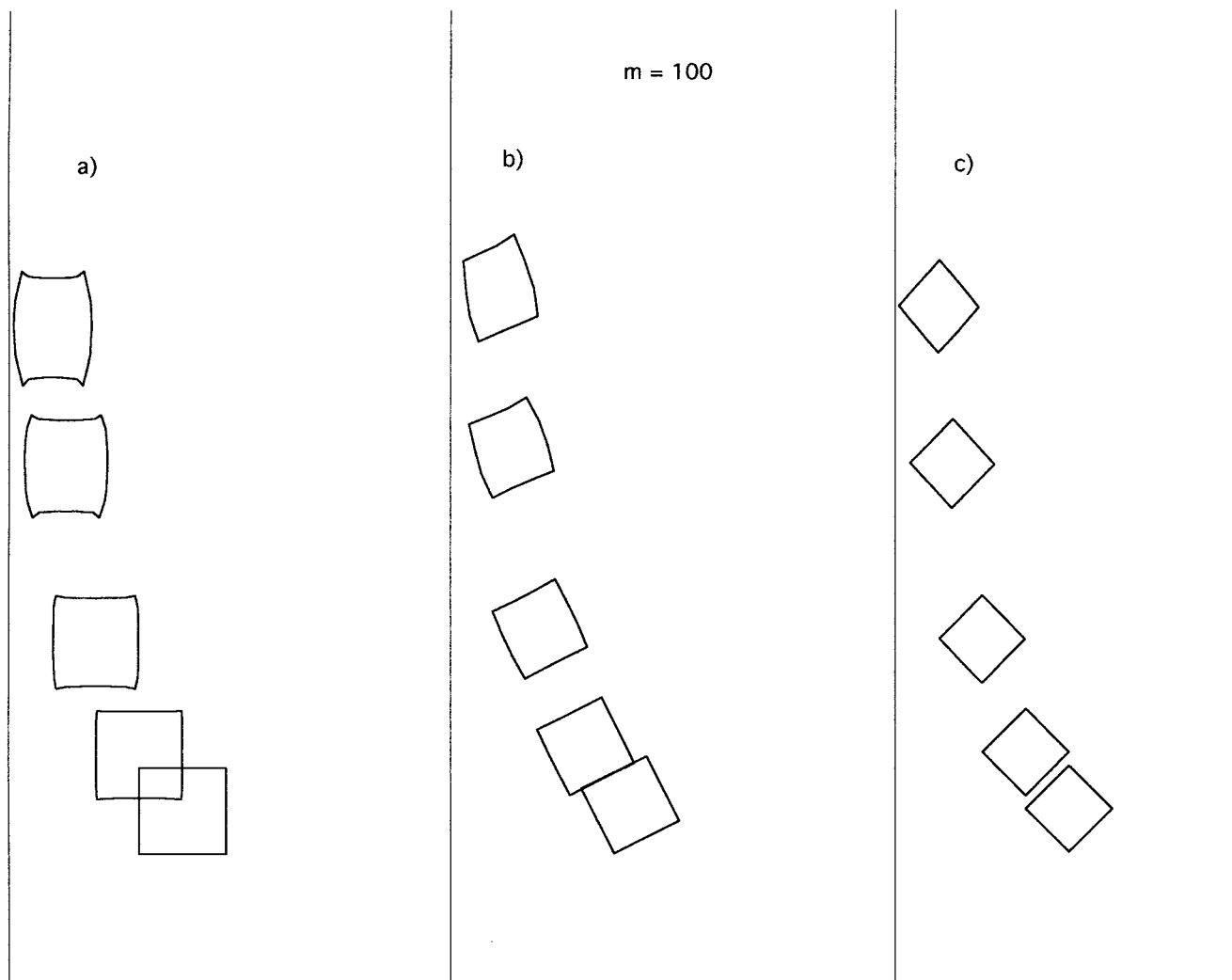
m = 100

a)   b)   c)

Fig. 4. As Fig. 3, but $m = 100$; highly competent objects.

mation, as the stiff object becomes increasingly close to the model edge (Fig. 4a), the object is eventually 'forced' to deform, irregularly. At these amounts of deformation, the object/matrix spacing approaches the object diameter value, which probably explains this gradual change from the expected semi-rigid behaviour for a high viscosity ratio, to deformation that might be expected if objects impinged. This change is seen for all three orientations, but the 'squares' in (a) show significant shape irregularity, whereas the 'rhombs' in (c) remain straight-sided while deformed, and the 'skew squares' in (b) fall in between.

For a viscosity ratio of 10 (Fig. 5), the object shape changes and strain are more clearly noticeable. The 'square' models produce progressive barrel shapes comparable to boudins, as described by Treagus et al. (1996) (but note that all the earlier models were only 50% shortened, equivalent to our middle rows). At high strain, these barrels show distinct 'fish mouth'

ends. Asymmetric barrel and flag shapes are seen for the 'skew square' models (Fig. 5b), whereas the 'rhombs' show increasing strain but only very slight shape irregularity (concave-sided). Comparison with Fig. 3 shows that all the objects have smaller average strain than passive objects that record the bulk strain.

The third example in the competent model series has $m = 5$ (Fig. 6). This is illustrated because the preliminary results in Treagus et al. (1996) suggested this to be the viscosity ratio that produces the *maximum* shape irregularity for competent objects. Whether this is substantiated by the new models will be examined quantitatively, later. The shapes shown in Fig. 6 have the same trends as those for $m = 10$, but are more elongate and more irregular. The lengthening sides become convex, and shortening sides strongly convex inwards. However, the $m = 5$ 'rhombs' again depart only slightly from rhombic, so their concave sides are hardly visible.
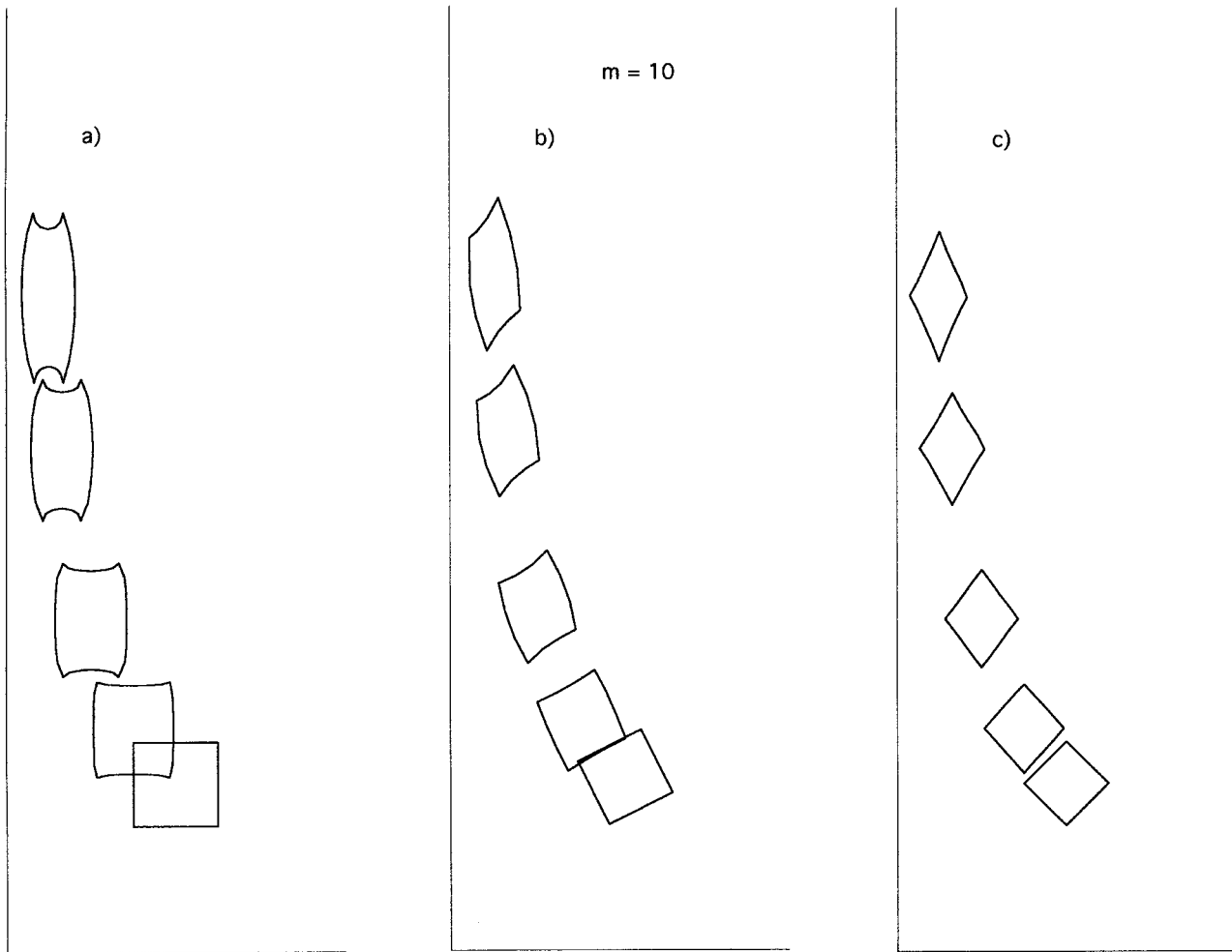
Fig. 5. As Fig. 3, but $m = 10$; competent objects.

3.2. Incompetent objects

Fig. 7 presents the models for $m = 0.1$; the results are very similar (as discussed above) for $m = 0.2$, 0.1 (shown), 0.01 and less. Comparison with Fig. 3 shows that all the objects deform by more than the passive objects, but the differences in elongation are not as great as might be expected. Discussion about 'incompetence' and its limiting effects, raised by Treagus et al. (1996) from the examination of theory for circular objects and the early models, is endorsed in Fig. 7 and the fuller compilation in Fig. 8. Even where $m \rightarrow 0$, the object axial ratios do not become infinitely large, but can be expressed as small numerical factors of the bulk strain ratio, as shown later.

The incompetent 'squares' in Fig. 7(a) show shapes progressing to spatula, bone and lobate ribbons, with progressive deformation. Whereas the shortening edges become excessively outward-bulging, the lengthening edges remain almost straight, giving an eventual smooth pseudoelliptical shape. The 'skew squares' in

Fig. 7(b) become irregular hooked parallelograms or 'string bean' shaped, with only slightly convex shortening sides, and concave lengthening sides. The 'rhombs' (Fig. 7c) show even less shape irregularity, best seen for the first deformation increment where the sinuous edges give the object a very slight lemon-shape. At high deformation, the differences seen between the three orientations are that the square has become an elliptical-ended ribbon, whereas the skew and diagonal squares remain highly angular.

3.3. Compilation and summary

The distinct features of the models in Figs. 3–7, plus more models, are presented as composite summary diagrams for the square (Fig. 8) and skew square (Fig. 9) objects, omitting the final extreme deformation stage, $R = 16$. The most extreme irregular shape changes occur for the 'squares' (Fig. 8), demonstrating that when these objects have a viscosity contrast with the surrounding matrix, they deform very inhomogen-
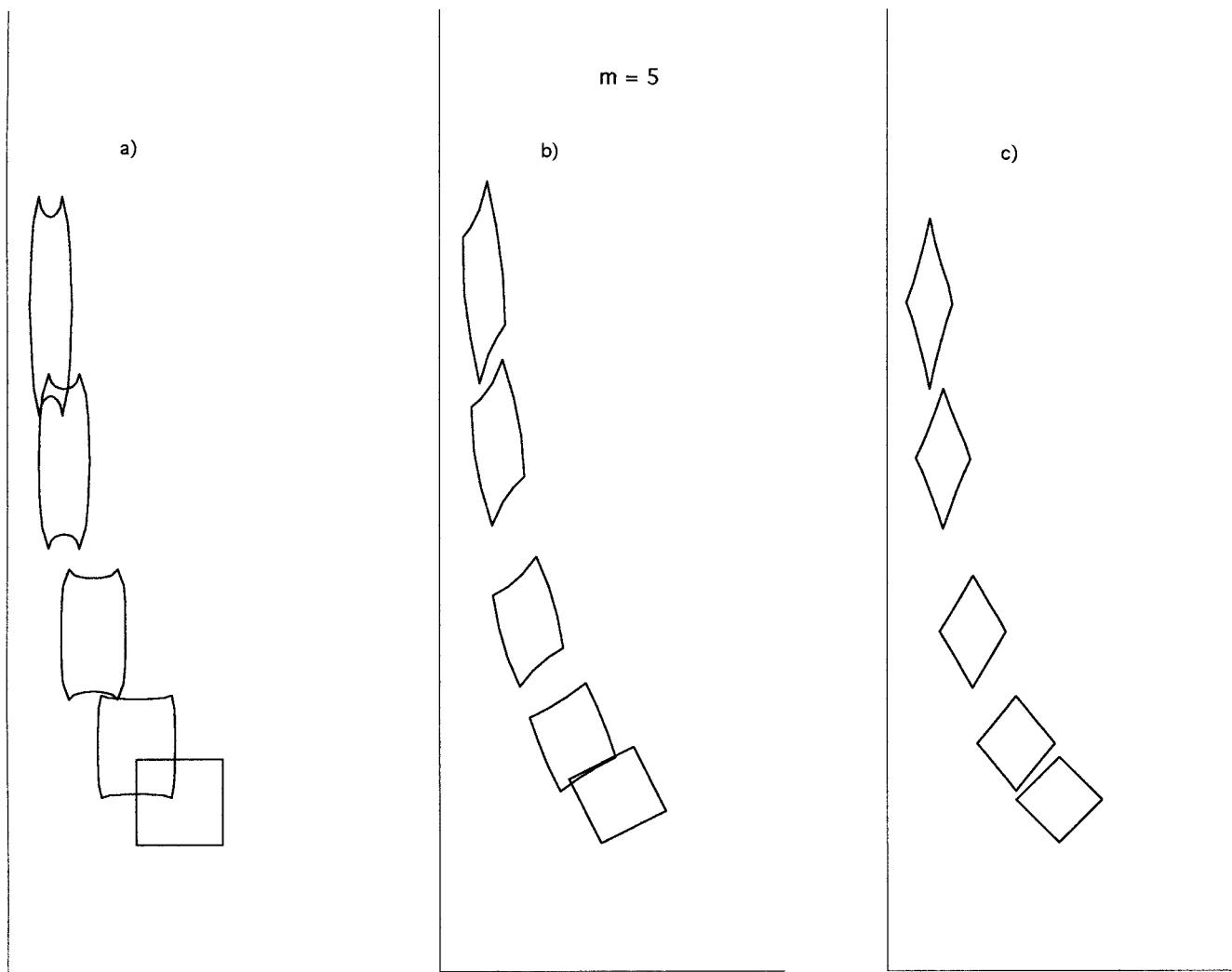
m = 5

a)

b)

c)

Fig. 6. As Fig. 3, but $m = 5$; moderately competent objects.

eously. The different geometric changes for competent and incompetent objects are clearly seen, even with small viscosity contrasts such as 2 or 0.5: i.e. concave-ended for competent objects, convex-ended, for incompetent. Ways of quantifying these effects will be given in a later analytical section.

The deformation of 'skew squares' produces comparable, but weaker, shape trends with viscosity ratio, as compiled in Fig. 9. The hooked or claw-like shapes for incompetent objects are not very sensitive to the m value (compare 0.2 and 0.1). The asymmetric barrel shapes of competent objects do not show the extreme 'fish mouth' ends seen for the 'squares', but the lengthening sides are convex, while the shortening sides are concave. Because these shapes are less distinct and extreme than those seen in Fig. 8, the interplay of elongation and irregularity gives rise to less distinctive paths. For example, the

$m = 5$ object in 50% bulk shortening (Fig. 9b) appears very similar to $m = 10$ at 67% bulk shortening (Fig. 9c). Perhaps the most notable features of the results summarised in Fig. 9 are the distinct asymmetric shapes that might mislead the eye into viewing them as 'shear criteria'. Yet all these object shapes arose in pure shear orthogonal to the page, and the 'shear' arises jointly from the asymmetry of these objects in pure shear and the heterogeneous effects due to viscosity contrasts. The question of strain orientation in these skew objects will be addressed in a later section, where it will be shown that the object strain is oblique to the bulk strain.

The 'diagonal square' objects deform approximately into rhombs, as already described. The shape variations are too slight to be useful viscosity indicators, and so are not repeated in a compilation diagram, here.
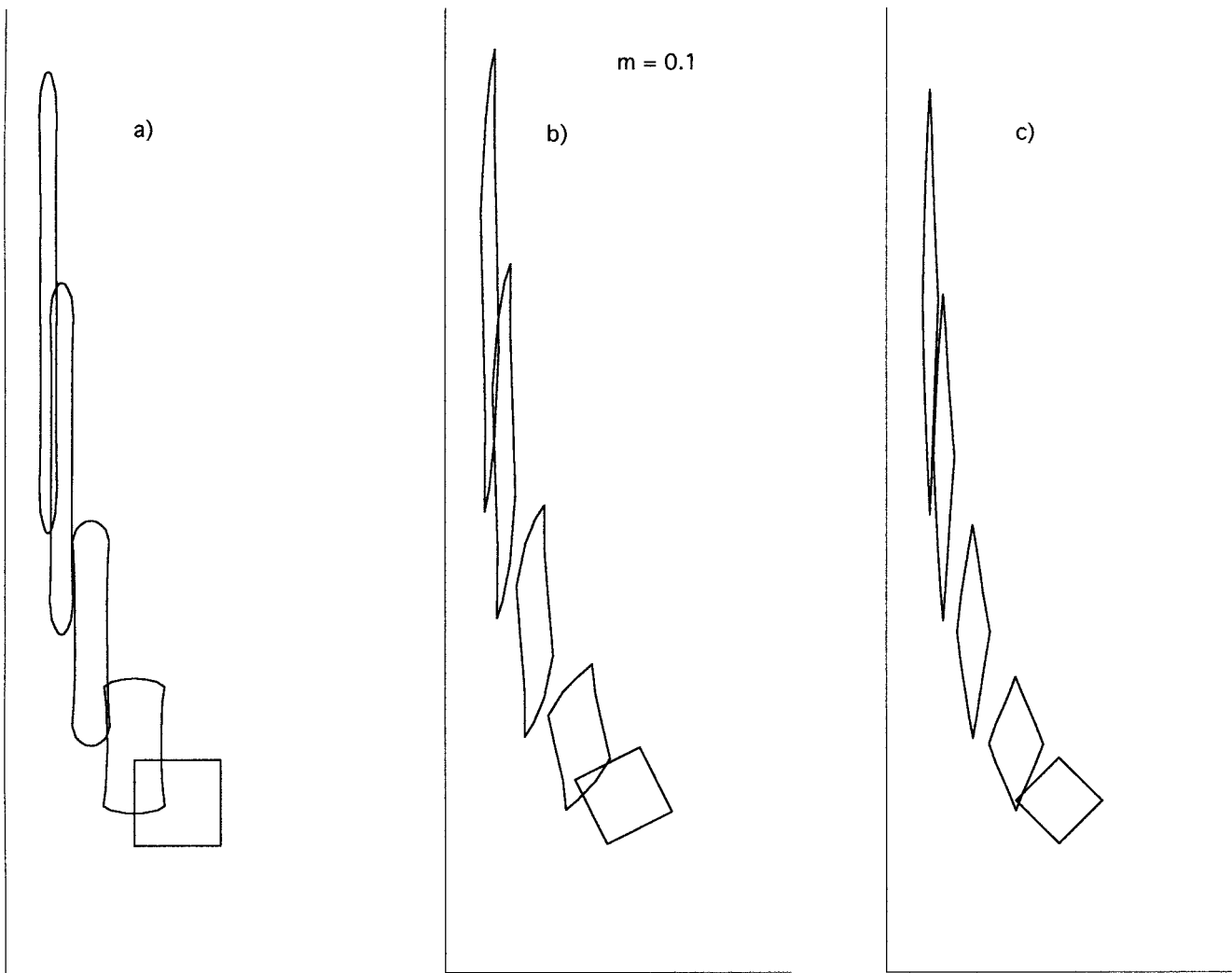
Fig. 7. As Fig. 3, but $m = 0.1$; incompetent objects.

4. Object strain analyses

4.1. Methods of analysis

The qualitative features of object strain and shape have been described above, in conjunction with Figs. 3–9. How might these be quantified, with the ultimate aim of applying the results to geological strain objects? The strains for the 'rhombs' are virtually homogeneous, and so the easiest of all to define and measure. However, for the 'squares' and 'skew squares', the shapes are irregular, demonstrating heterogeneous deformation. This is most evident in the barrel and bone shapes (Fig. 8), for which many different average strain ellipses might be drawn, within or enclosing the objects. Fig. 10(a and b) shows two chosen methods of measuring a barrel *object axial ratio*. The first, defined as *Rectangular R*, is the rectangular 'frame strain' (a/b) defined by the original corners

(Fig. 10a). The second, *Inside R*, is derived from measuring the inner axial ratio, a'/b' (Fig. 10b), equivalent to the average strain ellipse that would arise from a circle initially transcribed within the square object. It records the minimum barrel strain ratio, and does not take account of the heterogeneous deformation localised at the object corners. These R measurements will be compared.

We choose Rectangular R as the main measurement, because it affords the best method of comparing the object 'frame strain' for all three model series: 'squares', 'rhombs' and 'skew squares' (Fig. 10a, c and d). The original square corners are used, for each. For 'squares' and 'rhombs', the ratios (a/b) are determined from model output, directly. For the skew models (Fig. 10d), the average 'frame strain' needs to be calculated. This has been done for a limited number of models, using measurements of the deformed objects and Mohr diagram constructions. A Mohr diagram
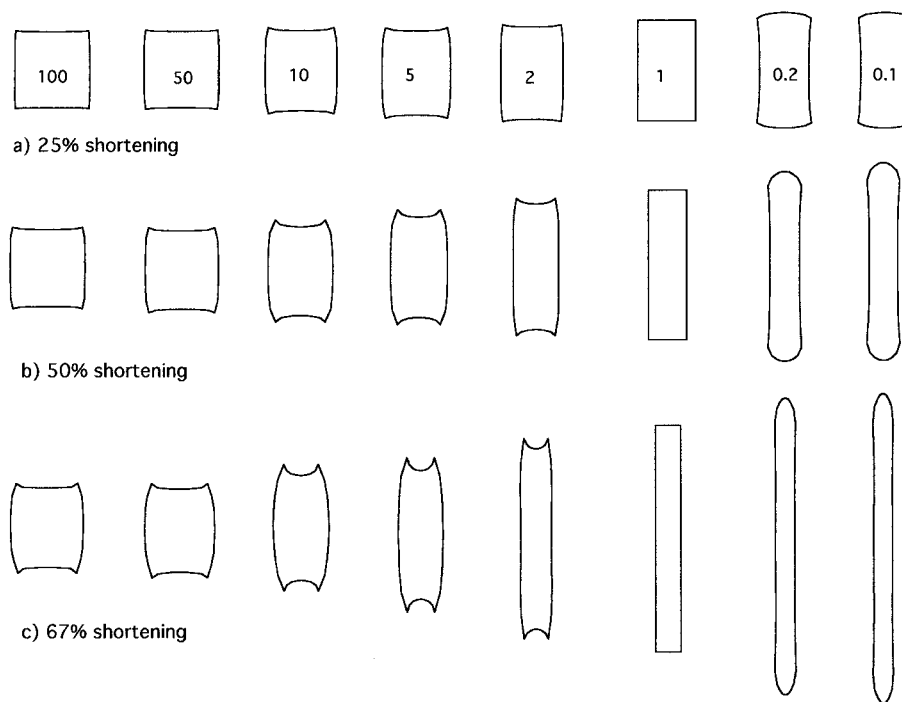
Fig. 8. Compilation of shapes of 'squares' for the first three stages of deformation, taken from Figs. 3–7 and other models. Note the distinct shapes and varieties of barrel and 'fish mouth' shapes, for $m = 2$, 5 and 10, and the decreasing object strain as m increases. Less variations of shape occur for $m < 1$, but with progressive deformation, shapes progress from bones to smooth lobate-ended strips that conceal the original square shape.

for stretch and rotation (De Paor, 1983; Means 1983; see also Treagus 1995) is particularly convenient, as the orientations and lengths of the frame sides (Fig. 10d, broken lines) provide two measures of stretch and rotation. Because these lines were originally orthogonal, they plot as a diameter on the Mohr circle for forward deformation, so identifying its principal axes to give the object strain ratio, R. It should be noted, however, that these R calculations are less accurate than those derived directly for 'squares' and 'rhombs', from object co-ordinate information. Calculations have not been made for $m > 10$ because the strains are considered too small to give an accurate result.

4.2. Object strain paths

Results for object strain versus bulk strain for the three types of square models are presented in Fig. 11(a–c), for $m = 0.1$, 5, and 10 (also 100 in Fig. 11a). This figure uses log–log R-graphs, as traditionally used for representing theoretical values for circular objects (see Introduction and Eq. 1). Accordingly, Fig. 11(d) presents theoretical results for circular to elliptical objects for comparable values of m (but $m = 100$ is omitted, as the curve is virtually on the abscissa). For competent square objects, in all three orientations (Fig. 11a–c), the curves are slightly upwardly concave, indicating increases in incremental object strain rate

with progressive strain. For incompetent objects, the curves vary from almost linear for 'squares', to a slightly decreasing gradient for 'rhombs' (a decreasing incremental strain rate). These trends are comparable to those noted earlier for circles (Fig. 11d).

If all these objects had deformed incrementally in steady state, at a *constant* factor of bulk incremental strain, expressed as:

$$\varepsilon_O = k\varepsilon_B, \tag{2}$$

where ε are natural (logarithmic) object and bulk strain rates, and k is a constant for the system (related to m and to shape), this would give rise to a *finite relationship* of the form:

$$\ln R_O = k \ln R_B; \quad \text{or } R_O = R_B^k. \tag{3}$$

This would be seen in linear m-curves on log–log R graphs (Fig. 11), which is not the case for any of the square models. Note that the curves for circular objects (Fig. 11d), based on Eq. (1) (Bilby et al., 1975) are also non-linear for $m < 1$, but approximately linear for $m > 1$ (competent objects), approaching the relationship previously determined by Gay (1968a), a form of Eq. (3).

Fig. 12 presents the strain results in Fig. 11, but now on linearly scaled R axes, and an interesting result emerges. For all three square orientations, plus circles in

a) 25% shortening

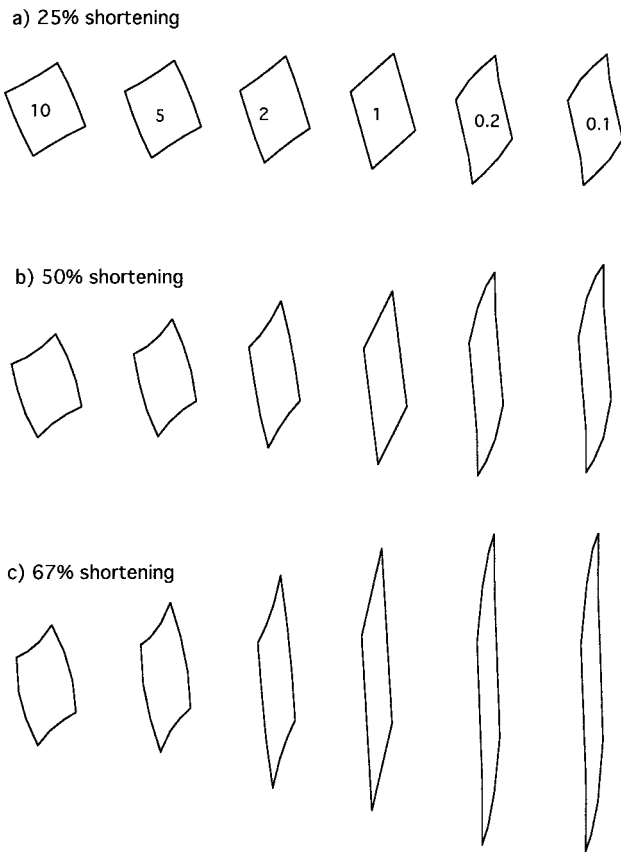b) 50% shortening

c) 67% shortening

Fig. 9. Compilation of shapes of 'skew squares' for the first three stages of deformation, taken from Figs. 3–7 and other models, for comparison with Fig. 8. Note the distinctly skew barrel and flag shapes for competent objects, and hook-like or 'string bean' shapes of incompetent objects. All remain quite angular in shape.

Fig. 10. Methods of measuring object 'average strain'. (a) Rectangular axial ratio, $R = a/b$, used in subsequent analyses of 'squares'. (b) Inside axial ratio $= a'/b'$. (c) Rhomb axial ratio, a/b. (d) Parallelogram defining outline of 'skew square' for strain analysis by Mohr diagram method.

theory, the m-curves are virtually linear; and this result is confirmed by other m values, not shown. The data are plotted from $(1, 1)$ on linear R scales, and so these results can be summarised as the approximate relationship:

$$(R_O - 1) = q(R_B - 1) \qquad (4)$$

where q is a constant factor, for a particular viscosity ratio and orientation of square (or circle).

Recall that circular inclusions deform homogeneously into ellipses, which is not the case for the square objects shown in Fig. 12, especially (a). Nevertheless, the strain paths for irregularly deforming squares, and more regularly deforming rhombs and circles, show similar near-linear trends in Fig. 12, fanning out from least strain for higher m values to a maximum strain for incompetent objects as $m \to 0$. These graphs show that for $m = 10$, q is about 1/3 for a 'square' (Rectangular R), 1/12 for a 'rhomb' and 1/22 for a 'circle'. For $m = 0.1$, q is 1.4 for a 'square', 1.7 for a 'rhomb' and 2.4 for a 'circle'. For the $m = 0$ circle, q is approximately 2.6, and this marks the 'limiting incompetent strain'.
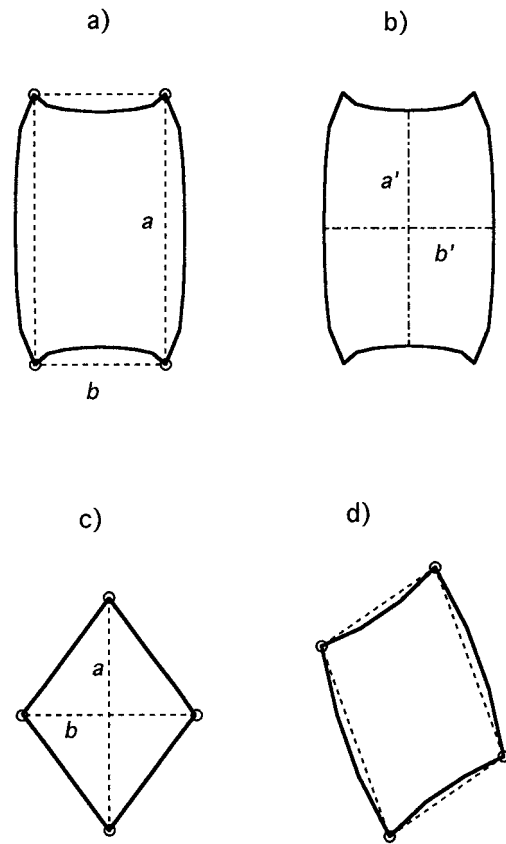
We have no simple explanation for the approximate linear relationship given in Eq. (4). It is possible that the developing inequancy of object shape affects the incremental deformation in a way that gives rise to this simple finite result. The non-linear trends in the log–log graphs (Fig. 11) are suggestive of a change from *active* competence-contrast behaviour, to progressively more *passive* incremental behaviour with increasing bulk deformation. The theoretical curves for elliptical objects (Fig. 11d), shown to higher strains in Bilby et al. (1975, fig. 2), suggest that threshold R_O values of 5–10 might mark onset of 'passive' behaviour. However, further modelling is needed to assess whether any universal object axial ratio can be defined, that applies to squares as well as circular objects, for onset of passive incremental deformation.

4.3. Effect of square orientation on strain

The results shown in Fig. 12 are compared in Fig. 13 directly, for three m values and models of 'squares', 'skew squares', and 'rhombs' (solid lines). Note, from
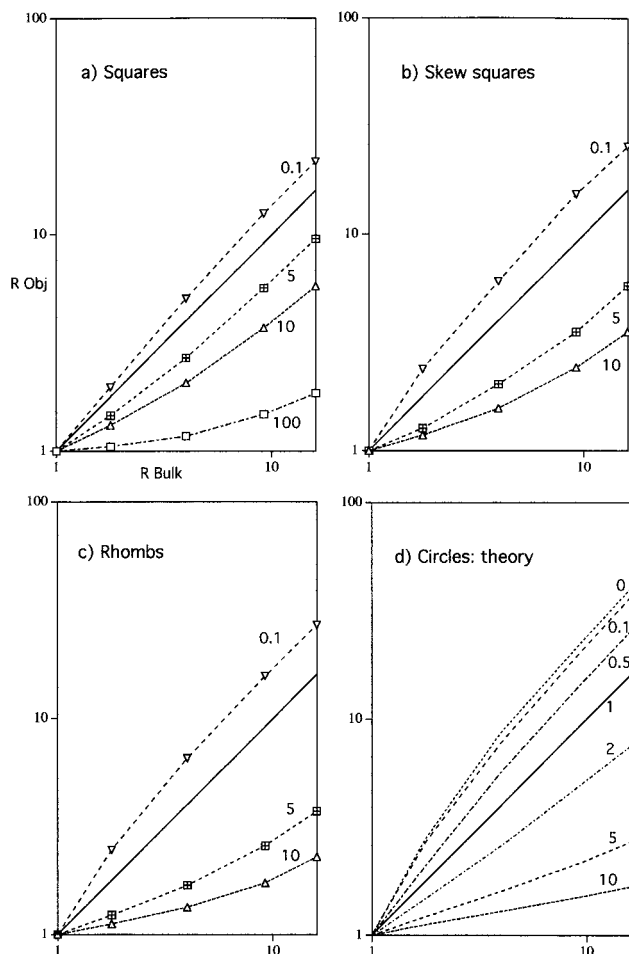
characterised by Rectangular $R = a/b$ (Fig. 10a). However, this is not the only way to measure the average object strain, as discussed earlier. Fig. 13 also shows the Inside R measurements (Fig. 10b) for the three m values, for comparison. For the competent barrels, Inside R is always less than Rectangular R, and vice versa for the incompetent objects. These differences are addressed in more detail in the next section, but we note here that Inside R produces virtually linear curves on these $(R - 1)$ graphs (Fig. 13). The values are only slightly different from the R values for rhombs, but systematically greater for competent *and* incompetent models (by about 10% and 6%, respectively). If Inside R were exactly the same as Rhomb R, this would mean that the barrels and bones had deformed in their inner (rhombic) half-area in just the same way as the rhomb object constructed in this way (see Fig. 1b). This is not quite the case, but sufficiently close to confirm that the deformation in the inner rhombic portions of 'squares' is more uniform than

Fig. 11. Graphs of object axial ratios (R Obj) versus bulk strain ratio (R Bulk) on log axes. (a) Rectangular R for 'squares' (defined Fig. 10a). (b) Calculated R for 'skew squares'. (c) R for 'rhombs' (Fig. 10c). (d) The equivalent graph for circles that deform uniformly into ellipses (Eq. 1). For all graphs, the curves are drawn and numbered for viscosity ratios, m (ranging from 100 to 0.1), axis labels (b)–(d) as (a), and the symbols in (a)–(c) indicate data points for FE models at the four stages of bulk deformation; see Figs. 3–7 for examples.

earlier, that the R values for 'skew squares' are less accurate than for the 'square' and 'rhomb' models; but nevertheless, the virtually linear relationship of $(R - 1)$ for object versus bulk strain is revealed in all cases.

The greatest competence contrasts (most different from bulk R) are recorded by diagonal squares (rhombs), the least differences for the squares parallel to pure shearing (as defined by Rectangular R), and the skew squares are intermediate. For example, the strain ratio given by the $m = 10$ square is roughly comparable to $m = 5$ for a skew square, $m = 3$ for rhombs, and nearer to 2 for circles. Of the three square orientations, the rhombs behave nearest to circles, but record less competence contrast (Fig. 13).

These comparisons all concern the 'frame strain' defined earlier, where the irregular 'squares' are
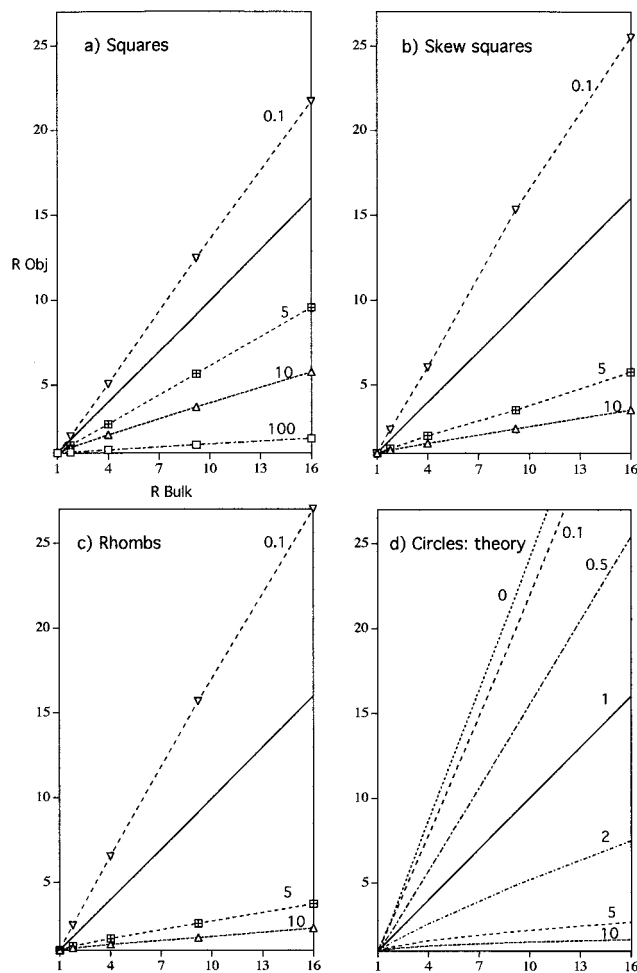

Fig. 12. As Fig. 11, but drawn on linear R axes, (b)–(d) axes as (a). Note that the curves shown in Fig. 11 are all now approximately linear.
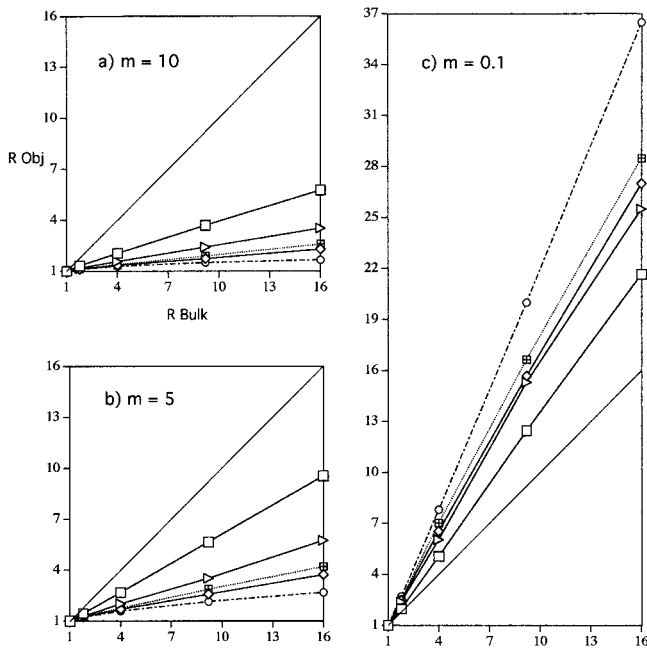
Fig. 13. Comparisons of object versus bulk strain data for three square orientations (solid lines) and circles in theory (dot–dash), for *m* values of (a) 10, (b) 5 and (c) 0.1, and linear *R* axes. (b)–(c) axes as (a). The square, rhomb and circle symbols indicate like-named models and their FEM data points; triangles symbolise the 'skew squares'. The crossed squares with dotted curves record Inside *R* for 'squares' (see Fig. 10b), and show the closeness to rhomb *R* values.

the outer corner regions, which are pulled out or in, to form the characteristic irregular shapes.

4.4. Sensitivity of object strain to viscosity ratio

The different ways of measuring an average object strain for the irregular 'squares', introduced above, are addressed in greater detail in Fig. 14 in terms of viscosity ratios. Fig. 14 compares (a) Rectangular *R* with (b) Inside *R*, documenting the variation of each with *m* for the four stages of model deformation. Rectangular *R* is always more than Inside *R*, for competent objects (barrels), and vice versa for incompetent objects. The lower-left diagram in Fig. 14 is especially useful to illustrate the very small differences for incompetent objects, over several orders of *m* magnitude (note plateau curves). In view of the similarity of the strain ratios of 'rhombs' to the Inside *R* for 'squares', noted above, the curves for the latter in Fig. 14(b) may also be taken as approximate values and trends for object strain versus viscosity ratio of 'rhombs'.

The relationships of Rectangular *R* and Inside *R* for 'squares' can be quantified as an *R-ratio* (Fig. 15), providing both a measure of object strain heterogeneity and of shape irregularity. The two are interrelated, as the barrel and lobate shapes arise because of these objects' departure from homogeneous deformation.
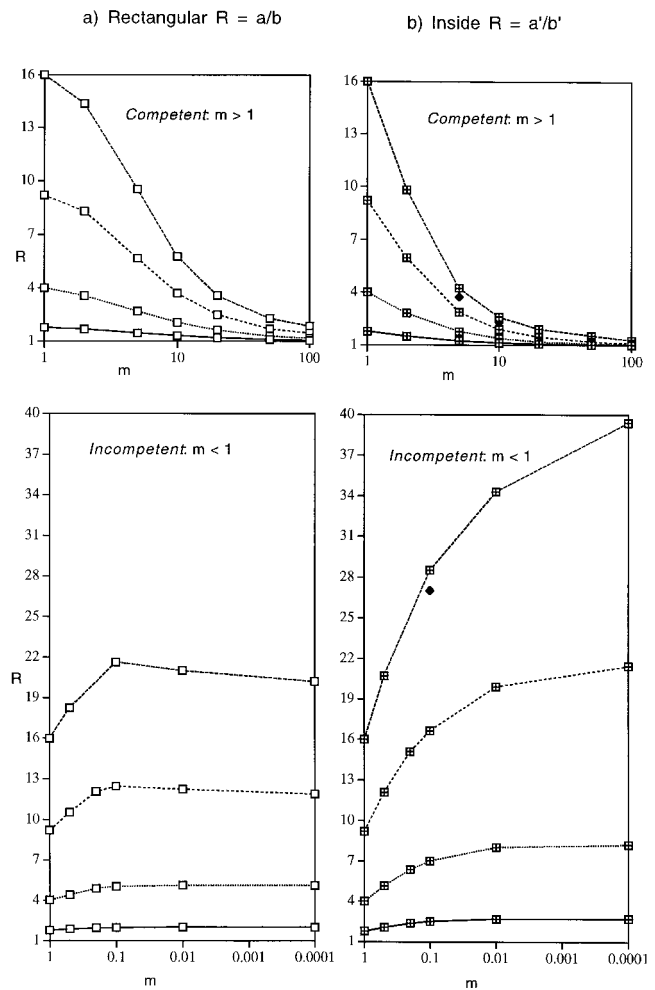

Fig. 14. Variations of (a) Rectangular *R* (squares) and (b) Inside *R* (crossed squares) for 'squares', plotted against *m* values. The symbols indicate model results, and the four curves represent the four successive stages of bulk deformation (*R* = 1.78, 4, 9.18, 16). Upper graphs *m* > 1 (competent objects); lower graphs *m* < 1 (incompetent). The solid diamonds superimposed on (b) show comparative *R* values for 'rhombs', for the fourth stage, for *m* = 0.1, 5, 10 and 20 (obscured), indicating closeness of Inside *R* and Rhomb *R*.

The shape features of the models will be discussed in more detail in the next section, but three main points emerge for *R*-ratios versus *m*, in Fig. 15. (1) For competent squares, the ratio broadly increases with progressive deformation, indicating growing heterogeneous strain. (2) The maximum irregularity and heterogeneous object strain in the competent objects is clearly revealed to be in the region of *m* = 5, for all four stages of deformation. (3) For incompetent objects, the curves are less distinct, and relatively insensitive to *m*.

4.5. Strain and rotation in skew models

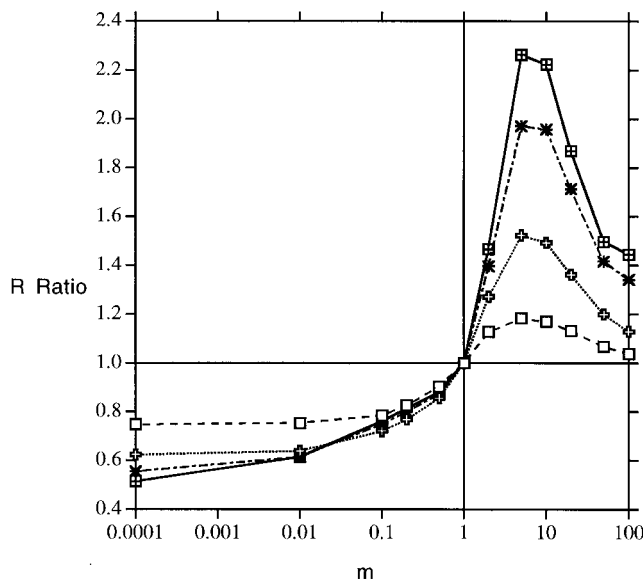Much of the previous analysis has concerned deformation of square objects in 'square' or 'rhomb' orien-

Fig. 15. *R*-ratio versus *m* graph: the ratio of Rectangular *R* and Inside *R* for 'squares', using data from Fig. 14. The four successive curves (squares, crosses, asterisks and crossed-squares), respectively, denote the four stages of bulk deformation ($R = 1.78, 4, 9.18, 16$). Note strong variations for $m > 1$, peaking near 5, compared to indistinct curves for $m < 1$.

tation with respect to bulk pure shear, and their comparison. The determination of object strain in the asymmetric 'skew square' models (see Fig. 9) was made by calculation rather than direct measurement. The object *R* values, discussed earlier, were shown to fall between the values for the squares and rhombs (Figs. 12 and 13). But what are the orientations of the object strain axes? It is obvious that the long and short axes of the object strains (however measured) for the symmetric squares and rhombs will be parallel to the bulk strain axes, because of their symmetry. So here the deformation is a pure shear, different in intensity but parallel in orientation, to the bulk pure shear. This cannot be assumed for the asymmetric objects in Fig. 9. Although these skew squares were originally equant objects, they were asymmetric: so what is the effect of their developing asymmetry on the deformation?

The $m = 100$ example (Fig. 4b) shows virtually zero rotation, as would be expected for pure shearing of a rigid object of this shape (Ghosh and Ramberg, 1976). What might be expected for an oblique angular object that deforms, differently from the matrix, is less obvious. The Mohr diagram method provided us with approximate strain ratios, discussed earlier (Figs. 11b and 12b), and also allows a fuller analysis of progressive deformation in these models. On- and off-axis Mohr circles of this kind can be used to show the differences between co-axial and non-coaxial deformation (Passchier, 1988). Our data show only small angles off-axis, from 1 to 4°, for all the examples: insufficient to distinguish margins

of error from slightly non-coaxial deformation, though more probably the former.

A more reliable measure of the deformation histories is to consider orientations of the original object edges to object principal axes, for the four stages of model deformation. The original orientation of the lengthening object edge to the bulk extension is 26.6°. From the Mohr diagram solutions for $m = 10$, the equivalent angles are found to be $18 \pm 1°$; for $m = 5$, $19 \pm 1°$; and for $m = 0.1$, $29 \pm 1°$. Importantly, there is no consistent change through the four deformation stages, which implies that the principal axes for the object strains are all material lines, and so their deformations are coaxial. Clearly, these angles are different from the edge orientation of 26.6° quoted above for bulk strain and passive behaviour, and we interpret this to mean that the average deformation within the skew square objects must be a pure shear *oblique* to the bulk pure shear. For $m = 10$ (Fig. 5b), the object extension acts 8.5° anticlockwise of the bulk extension (long axis); for $m = 0.1$ (Fig. 7b), it is just 2.5° clockwise.

In summary, the average strain in these skew square objects has *R* values within the range reported for rectangular *R* for 'squares' and 'rhombs;' but it appears that they do not deform with axes parallel to the bulk strain, if there is a viscosity ratio. The stiffer the object, the more the extension direction is refracted towards the directions of original object-edges. The incompetent objects only show a small amount of refraction of pure shear axes, this time in the sense of the lengthening object diameter. These are preliminary and tentative results that will be investigated more thoroughly in ongoing work, but they appear to share some of the features of strain refraction already described for layered systems (Treagus, 1988).

5. Analyses of object shapes and irregularities

The preceding analyses considered ways of quantifying overall object strains, while noting that the 'squares' model series strained heterogeneously into varieties of barrel, bone or lobate shapes (Fig. 8). It was noted, earlier, that equivalent circular or elliptical objects would deform homogeneously, even if there were viscosity contrasts, with all the necessary heterogeneity of local strain accommodated in the matrix region around the object: not in the object itself. It has already been seen that the orientation of the original non-elliptical shape (in this case, square) is an important control on the heterogeneity of strain, and the resulting shape changes. Comparing the irregularity of model 'squares' (becoming barrels and bones) and model 'rhombs' (becoming near-rhombs) suggests a more general result: *that objects with viscosity contrast will deform most irregularly where they have straight edges sub-parallel to the shortening*
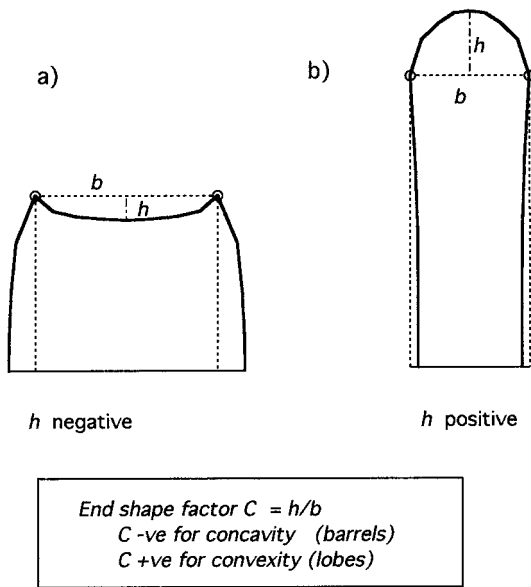
Fig. 16. Definition of normalised end-shape factor, C, for 'squares'. (a) Negative C measures concavity in a barrel with 'fish mouth' ($m = 10$; bulk $R = 4$). (b) Positive C measures convexity for lobate incompetent object ($m = 0.1$; bulk $R = 4$).

direction. This is borne out by our models with various other object shapes.

The present analyses will concentrate on the 'square' models (parallel to strain axes) and their characteristic

Fig. 17. Relationship of concavity/convexity, $|C|$, to R values in 'square' objects with different m values (labelled). (a) $-C$ versus bulk R in competent objects; (b) $-C$ versus object R (rectangular) in competent objects; (c) C versus bulk R in incompetent objects. Symbols indicate model data points, and numbers m values.

shape features. Two approaches to measurement of shape irregularity of barrel and bone shaped objects will be presented. One concerns the R-ratio of the two strain measures (Rectangular R and Inside R) discussed above and graphed in Fig. 15. This figure showed a maximum R-ratio for the $m = 5$ model; a result noted in the earlier results at 50% bulk shortening (Treagus et al., 1996), and now confirmed over four stages of model deformation. (However, $m = 5$ may not be the exact maximum.) The second is a more direct measure of concave and convex shape effects, addressed next.

The characteristic shapes compiled in Fig. 8 arise principally through concaving or convexing of the shortening object edges, according to the viscosity contrast. We introduce (Fig. 16) a dimensionless measure, C: a ratio of the maximum relative displacement of the edge, given by h, and the rectangular width, b. C is negative for concavity (e.g. fish-mouth ends of barrels), and positive for convexity (e.g. lobate end of bones).

Fig. 17(a) shows C-factors versus bulk R curves for the competent model series. This endorses the noted result that the maximum irregularity occurs for the $m = 5$ models. (However, other analyses suggest that the true value for maximum irregularity may be in the range of $m = 3$–4.) The stiffest objects fall close to the abscissa, which represents a *straight* edge, and this occurs also for $m = 1$. Thus the m values fan upwards from $m = 1$–5, and downwards again to $m > 100$. To separate these data, Fig. 17(b), shows C versus object strain (Rectangular R), and clear trends with slopes related to m now emerge. The values for $m > 10$ are omitted, here, because these data cluster along the $m = 10$ line, ever closer to the graph origin as m increases. An equivalent graph of C for incompetent 'squares' versus bulk R (Fig. 17c), shows a consistent variation from the abscissa ($m = 1$) to maximum at $m = 0.0001$. These data have not been shown additionally as C versus object strain, but earlier figures allow conversion of Bulk R to the object R values, if required.

All the shape analysis graphs in Fig. 17 show approximately linear trends of $|C|$ with $(R - 1)$, demonstrating a progressive steady growth of concavity/convexity as a factor of bulk and object strain. This was maintained even in models at the highest bulk strains, where there might arguably be insufficient matrix to surround and accommodate the objects steadily. The consistent linear trends, both for the strain measurements noted earlier, and the normalized shape measurements given in Fig. 17, are quite surprising, and would seem to support the viability of even the most extremely deformed models. These results offer the prospect of using end-concavity/convexity as a new viscosity-ratio indicator for geological objects of this kind.
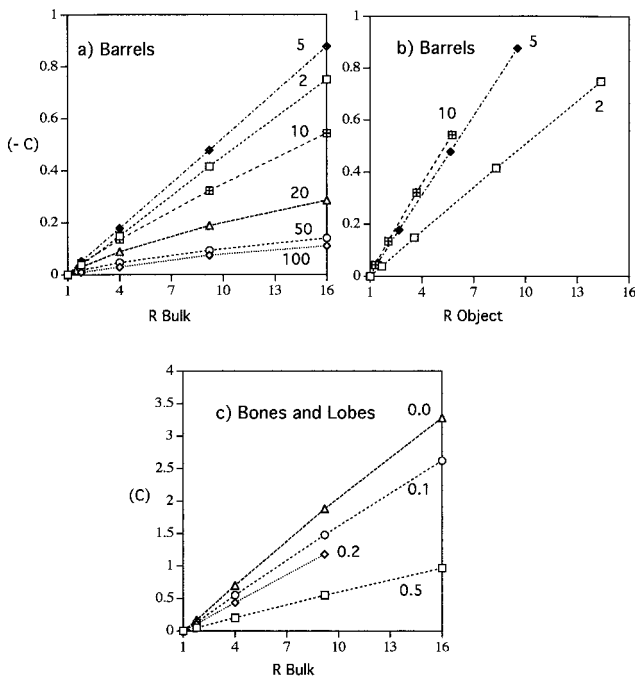
6. Implications and conclusions for geological strain analysis

6.1. Object shapes and geological clasts

The modelling presented in this paper concentrates on square objects, and how these deform when surrounded by a matrix of different viscosity. To be relevant to rocks, we need to be able to justify many things: (1) modelling object and matrix as Newtonian fluids with different viscosity, to simulate 'competence contrast' in rocks; (2) whether square objects are appropriate for modelling any kinds of geological clasts; (3) whether these single-object models can be applied to rocks that contain closely spaced clasts.

In the Introduction, we raised the question of clast shape in rocks and referred back to our earlier paper on this topic (Treagus et al., 1996). We noted that most traditional methods of strain analysis in rocks assume that strain markers behave passively (no competence contrast), and/or that the objects began as spheres or ellipsoids. We specifically questioned whether conglomerates, so commonly used for strain analysis (e.g. in R_f–ϕ analysis), have pebbles that are always ellipsoidal. And if not, what is the effect of initial shape on deformation?

A square object might not be any closer to a reasonable initial 'ideal' shape (in two dimensions), than a circle, for geological clasts. But it provides an alternative: a route to understanding the deformation of *any* angular object, which theory shows will not deform homogeneously if there is a viscosity contrast. There are a few kinds of clast that might be originally cubic or cuboidal: for example, prismatic crystal grains and feldspar clasts. In contemporaneous work (S.H.T. with J.E. Treagus), sampling and analysing many examples of deformed conglomerate, tillite and breccia in Europe, we have observed clasts with all manner of shapes: sometimes quite round, that could be reasonably approximated as elliptical; commonly angular, triangular to polygonal; sometimes suggestive of original equancy; but in many cases elongate in a manner that could be due to an initial prolate or oblate 3D shape, or due to deformation (or both). These observations raise one of the most difficult problems in analyses of such rocks: *how to determine strain if the original object shape is not known*. R_f–ϕ analyses (see Lisle, 1985) can avoid this problem by statistical sampling, if it can be assumed that with sufficient population of varied clasts, the sum total of all the individual clast shapes and orientations is 'uniform'.

The results in this paper take the opposite approach, by examining what might be revealed about rheology from *single* objects, using squares in different orientations. We have shown that the deformation arises by two interrelated processes, affecting squares in the

three model orientations in distinctly different ways. One process involves an average object strain, broadly proportional to viscosity ratio, as for circular objects: but notably different for the three modelled orientations. 'Square' competent objects record more than 'rhombs', largely due to greater strain at their corners, accentuating the cornered shape. The results for incompetent square objects show the opposite effect: while the angular shapes persist throughout the deformation of asymmetric and diagonal squares into skewed parallelograms and rhombs, the extreme heterogeneity of deformation for the 'square' orientation causes the angularity to disappear, and the object to become such a lobate-ended strip that all its original squareness has disappeared. The problem with such a shape, if this were a geological clast and its 'incompetence' and internal strain were not evident, is that it could appear to be a passively deformed round object.

6.2. Object and clast strain histories

The object strain measurements for our models reveal a special kind of steadiness of deformation, for all three square orientations, seen also for circular objects in theory and modelling. We found all the paths of $(R-1)$ of object versus bulk strain (including two different measures for the irregular 'squares'), to be approximately linear, given by the expression:

$$(R_O - 1) = q(R_B - 1),$$

where the gradient, q, is related to viscosity ratio, object shape and (if non-circular) orientation. This is a surprising result for finite strain relationships, with no obvious genetic explanation, but one that has potential for applying to geological objects of many shapes.

This empirical finite strain relationship between object and matrix may be masking what is happening incrementally. The non-linear relationships of log-R for object and matrix suggest an incremental strain history of increasingly passive behaviour with increasing strain. This may arise in the finite element models partly as a result of model design and boundary conditions, and their effects on object–matrix spacing: but this is probably not the main reason, as similar trends are seen in other models with different spacing, and in theory of circular objects which assume an infinite matrix. It would seem that the developing strain and inequancy of objects serve to reduce incremental competence contrasts, and it may be possible to define an object axial ratio, such as 5 or 10, that is an effective threshold value for passive behaviour (applicable only to long objects aligned parallel to the bulk extension). This would require fuller testing in further model and field-based analyses. The tentative conclusions for geological strain analysis of fragmental rocks, are (a) that

originally elongate clasts will deform more than equant clasts of the same lithology (whether round or angular); and (b) that the greater the bulk deformation, the more the whole rock may approach an appearance of homogeneous deformation.

A significant finding from the strain analyses of the 'skew squares' is that the object strains are oblique to the bulk strain: refracted measurably anticlockwise (with respect to the models in Fig. 9) towards the object edges in the stiff competent objects, refracted very slightly clockwise in the incompetent. This has implications for strain analysis, as it means that cleavage fabrics in angular clasts might not be parallel to cleavage in the matrix. However, the result is not surprising, as strain and cleavage refraction are recognised features of deformed contrastingly layered systems (Treagus, 1983, 1988). Initially slab or rod-shaped geological clasts might be expected to exhibit strain refraction similar to those modelled for layers (see also Treagus and Sokoutis, 1992). Nevertheless, we had not anticipated refraction into initially square but obliquely oriented objects, so this result suggests that angularity and asymmetry in orientation to bulk strain axes are sufficient to generate oblique strains, even in equant objects. This tentative conclusion will be investigated further through other models and ongoing field studies.

6.3. Shear criteria

A further feature of the asymmetric square objects is that the variably skewed shapes might appear rather like 'shear criteria', and might be misdiagnosed as features related to simple shear. Yet these were all produced in pure shear. In some preliminary finite element modelling of equivalent square objects in bulk *simple shear* deformation, we produced surprisingly similar results to those shown here. Geologists often use the theoretical behaviour of rigid objects of different shapes as a means of distinguishing the effects of pure and simple shear (or more generally, to indicate the vorticity) (Ghosh and Ramberg, 1976). Our preliminary results for deformable objects suggest that the differences at moderate strains might only be slight, but this will be pursued in further work.

6.4. Clast shape changes

Our FE model results reveal the potential for using clast shape changes as an indicator of competence contrast, and a possible way of measuring viscosity ratio in rocks. Ideally 'round' objects and pebbles will deform regularly and homogeneously into ellipses, whose strain is related to viscosity ratio; but angular objects provide an additional measure of this from their shape changes. From studies of a range of angular shapes not reported here, we consider *a straight edge initially sub-parallel to bulk shortening* to be the best indicator. We define a dimensionless measure of concavity/convexity (C) which appears from the 'square' models to have a linear relationship to $(R - 1)$ for a specific viscosity ratio.

These results are being used in current work (with J.E. Treagus), in analysing clast shapes in fragmental rocks: to see whether competence contrasts can be assessed in this way; and whether the method can be used to help quantify geological strains. From preliminary studies, we find a better potential for shape studies lies in the concavity of competent clasts and boudins, than in lobing of incompetent clasts, for the following reasons. (1) There are generally more quartzose or granitic clasts in conglomerates, breccias and tillites, which are clearly competent, than demonstrably incompetent clasts. (See later.) (2) There will be uncertainty about original clast shape for any lithology, but the extreme elongation and smoothing of incompetent objects makes it unlikely that any original straight edge parallel to shortening could be identified. Measures of concavity are thus being investigated in deformed conglomerates and breccias. While the extreme barrel shapes shown in Fig. 8 appear rare in the clastic rocks under study, there are many examples of slightly concave- and convex-sided fragments, including 'shield' shapes of triangular clasts, that are expected to yield information on the effective viscosity ratios among different rock types and their matrices.

6.5. Competence, incompetence and viscosity ratios in rocks

The results from these models and theory of object–matrix systems have relevance to the meaning of competent and incompetent behaviour of rocks in more general terms. We noted that the greatest shape irregularity for *competent* objects occurs for viscosity ratios in the order of 5; and that at higher ratios (> 20), objects behave more nearly rigidly. For layered systems (Treagus, 1983, 1988), viscosity ratios of 10 can give rise to significant changes in strain. In a newly proposed method for quantifying viscosity ratios in rocks from cleavage refraction angles (Treagus, 1999), it is suggested that the features of cleavage refraction attributed to competence contrasts could arise from very small viscosity ratios of 2–6. The present object–matrix modelling independently suggests that clasts that measurably deform must also be those that have quite small viscosity ratios, such as 2 and 5. Objects with viscosity ratios to matrix of > 10 will probably have behaved too rigidly to record measurable strain or fabric.

Incompetence would appear to be far more insensitive and difficult to quantify in rocks, despite its sometimes dramatic effects (Talbot and Sokoutis, 1992). Theory and modelling for object–matrix systems show

that even the most incompetent circular clast ($m = 0$) will record ($R - 1$) only 2.6-times the bulk value; and square clasts by 1.3 times. So geological clasts with a lower effective viscosity than surrounding matrix may appear to have deformed *almost as passive objects*. However, it then becomes difficult to assess whether an object is truly 'incompetent', or simply behaved rheologically in the same way as the matrix (i.e. no competence contrast). These are questions of importance in how deformation is partitioned among various rock types, whether in clast–matrix systems, in layers, or around folds, and might invite further discussion and research.

References

Bilby, B.A., Eshelby, J.D., Kundu, A.K., 1975. The change of shape of a viscous ellipsoidal region embedded in a slowly deforming matrix having a different viscosity. Tectonophysics 28, 265–274.

Bilby, B.A., Kolbuszewski, M.L., 1977. The finite deformation of an inhomogeneity in two-dimensional slow viscous incompressible flow. Proceedings of the Royal Society A355, 335–353.

De Paor, D.G., 1983. Orthographic analysis of geological structures—I. Deformation theory. Journal of Structural Geology 5, 255–277.

Eshelby, J.D., 1957. The determination of the elastic field of an ellipsoidal inclusion, and related problems. Proceedings of the Royal Society A241, 376–396.

Flinn, D., 1956. On the deformation of the Funzie conglomerate, Fetlar, Shetland. Journal of Geology 64, 480–505.

Freeman, B., 1987. The behaviour of deformable ellipsoidal particles in three-dimensional slow flows: implications for geological strain analysis. Tectonophysics 132, 297–309.

Gay, N.C., 1968a. Pure shear and simple shear deformation of inhomogeneous viscous fluids. 1. Theory. Tectonophysics 5, 211–234.

Gay, N.C., 1968b. Pure shear and simple shear deformation of inhomogeneous viscous fluids. 2. The determination of the total finite strain in a rock from objects such as deformed pebbles. Tectonophysics 5, 295–302.

Gay, N.C., 1976. The change of shape of a viscous ellipsoidal region embedded in a slowly deforming matrix having a different viscosity—a Discussion. Tectonophysics 35, 403–407.

Gay, N.C., Fripp, R.E.P., 1976. The control of ductility on the deformation of pebbles and conglomerates. Philosophical Transactions of the Royal Society A283, 109–128.

Ghosh, S.K., Ramberg, H., 1976. Reorientation of inclusions by combination of pure and simple shear. Tectonophysics 34, 1–70.

Hanson, B.H., 1990. Thermal response of a small ice cap to climatic forcing. Journal of Glaciology 36, 49–56.

Hossack, J.R., 1968. Pebble deformation and thrusting in the Bygdin area (S. Norway). Tectonophysics 5, 315–339.

Hudleston, P.J., Lan, L., 1994. Rheological controls on the shapes of single-layer folds. Journal of Structural Geology 16, 1007–1021.

Lan, L., Hudleston, P.J., 1991. Numerical models of buckle folds in non-linear materials. Tectonophysics 199, 1–12.

Lan, L., Hudleston, P.J., 1996. Rock rheology and angular folds in single-layers. Journal of Structural Geology 18, 925–931.

Lan, L., Hudleston, P.J., 1997. The effects of anisotropy on the shape of fault-bend folds. Proceedings of the 30th International Geological Congress, Vol. 4, pp. 106–118.

Lisle, R.J., 1985. Geological Strain Analysis. A Manual for the R_f/ϕ Technique. Pergamon Press, Oxford.

Lisle, R.J., 1988. The superellipsoidal form of coarse clastic sediment particles. Mathematical Geology 20, 879–890.

Lisle, R.J., Rondeel, H.E., Doorn, D., Brugge, J., van de Gaag, P., 1983. Estimation of viscosity contrast and finite strain from deformed elliptical inclusions. Journal of Structural Geology 5, 603–609.

Lloyd, G.E., Ferguson, C.C., 1981. Boudinage structure: some new interpretations based on elastic–plastic finite element simulations. Journal of Structural Geology 3, 117–128.

Means, W.D., 1983. Applications of the Mohr-circle construction to problems of inhomogeneous deformation. Journal of Structural Geology 5, 279–286.

Passchier, C.W., 1988. The use of Mohr circles to describe non-coaxial progressive deformation. Tectonophysics 149, 323–338.

Ramberg, H., 1955. Natural and experimental boudinage and pinch-and-swell structures. Journal of Geology 63, 512–526.

Ramsay, J.G., Huber, M., 1983. The Techniques of Modern Structural Geology. Volume I. Strain Analysis. Academic Press, London.

Selkman, S.O., 1983. Stress and displacement distributions around pyrite grains. Journal of Structural Geology 5, 47–52.

Shimamoto, T., 1975. The finite element analysis of the deformation of a viscous spherical body embedded in a viscous medium. Journal of the Geological Society of Japan 81, 255–267.

Talbot, C.J., Sokoutis, D., 1992. The importance of incompetence. Geology 20, 951–953.

Treagus, S.H., 1983. A new theory of finite strain variation through contrasting layers, and its bearing on cleavage refraction. Journal of Structural Geology 5, 351–358.

Treagus, S.H., 1988. Strain refraction in layered systems. Journal of Structural Geology 10, 517–527.

Treagus, S.H., 1995. Superposed deformations by Mohr construction. Journal of Structural Geology 17, 783–791.

Treagus, S.H., 1999. Are viscosity ratios measurable from cleavage refraction? . Journal of Structural Geology 21, 895–901.

Treagus, S.H., Hudleston, P.J., Lan, L., 1996. Non ellipsoidal inclusions as geological strain markers and competence indicators. Journal of Structural Geology 18, 1167–1172.

Treagus, S.H., Sokoutis, D., 1992. Laboratory modelling of strain variation across rheological boundaries. Journal of Structural Geology 14, 405–424.